



# Fixation strength of conformal additively manufactured Ti6Al4V implants in large animal model

David Downing<sup>1</sup> · Bill Lozanovski<sup>1</sup> · Tom Williamson<sup>1</sup> · Arman Namvar<sup>1</sup> · Endri Kastrati<sup>1</sup> · Dave Hill<sup>1</sup> · Darpan Shidid<sup>1</sup> · Ulrich Buehner<sup>2</sup> · Stewart Ryan<sup>3</sup> · Ma Qian<sup>1</sup> · Peter Choong<sup>4,5</sup> · Martin Leary<sup>1</sup> · Milan Brandt<sup>1</sup>

Received: 6 December 2023 / Accepted: 4 March 2024  
© The Author(s) 2024

## Abstract

Additive manufacturing (AM) enables patient-specific lattice-based implants with porosity engineered to encourage bone ingrowth and to mimic bone's mechanical stiffness. The strength of the bone-implant interface can be measured through a destructive 'push-out' testing. The aim of this study is to explore the effect of implant-bone stiffness ratio ( $\gamma$ ) on the push-out force using numerical simulation and a small experimental study. Numerical simulations of an implant-bone interface during a push-out test showed a fundamental change of failure mode for  $\gamma$  ranging from 0.1 to 10. For the geometry considered, the largest push-out forces were predicted for  $\gamma \approx 0.7$ , essentially doubling the push-out force compared to a solid titanium implant. The experimental and simulation results also demonstrated that using an intermediate stiffness metal implant lattice geometry,  $\gamma \approx 1.35$ , does not significantly improve the peak force of the push-out test compared to the solid implant. For the experimental study, critical-sized defects were simulated via robotic bone resection in the right lateral distal femur of a group of ~2.5-year-old healthy sheep, and then solid or lattice-based Ti6Al4V implants inserted. The femurs were harvested 6 months after implantation. Nine of the implanted femurs (six solid and three lattice-based) were used for fixation testing. The experimental study showed no significant difference in push-out force between a solid and moderately stiff lattice metal implant as indicated by the numerical simulation.

**Keywords** Additive manufacturing · Patient-specific · Lattice structure · Biomechanical testing

## 1 Introduction

Bone defects may include severe fractures or infection, which have a large array of classification (Fig. 1). Generally, a defect that is greater than 1–2 cm and causes a 50% loss in the circumference of the bone may be classifiable as 'critical-sized' [1]. For long bones, a reported defect size

of 20% of the length of the bone may also be classified as 'critical-sized' [2]. Surgical resection of bone tumours can severely compromise the integrity of the remaining healthy bone, requiring further intervention or reconstruction.

To assist healing of critical-sized defects, bone graft procedures such as allografts [3] and autografts [4] are typically employed. Bone grafts can suffer from donor site morbidity [5] and low union rates [6]. Additively manufactured, patient-specific biocompatible metal implants offer an alternative to bone grafts. These provide the geometric freedom to fill complex voids in the bone and include cellular structures to match bone load response and porous surfaces to promote bone ingrowth.

Robotic resection is increasingly utilised, due to increased geometric repeatability, for example in this research methodology (Sect. 2.4). For example, a 7.8 mm linear deviation improvement, 7.9° pitch and 4.6° roll angular deviation improvement were reported with a robot-assisted technique compared to the manual technique for resection of bone [7]. Other surgical procedures that have used robot resection

✉ David Downing  
david.downing@rmit.edu.au

<sup>1</sup> RMIT Centre for Additive Manufacture, School of Engineering, RMIT University, Melbourne, Australia

<sup>2</sup> Stryker Corporation, Sydney, Australia

<sup>3</sup> Faculty of Veterinary and Agricultural Sciences, University of Melbourne, Melbourne, Australia

<sup>4</sup> Department of Surgery, St. Vincent's Hospital, Melbourne 3000, Australia

<sup>5</sup> Department of Surgery, University of Melbourne, Melbourne, Australia

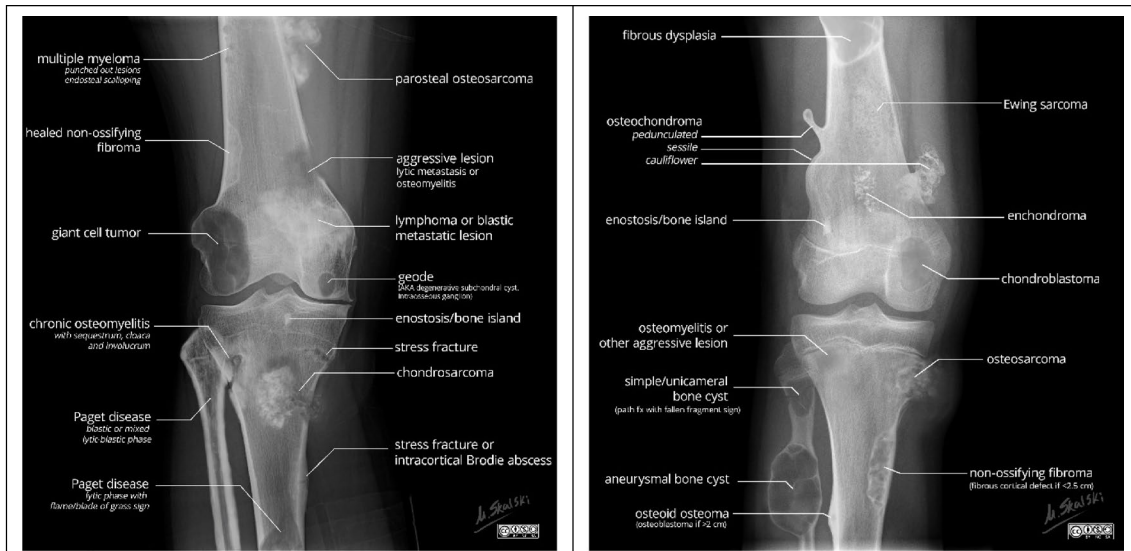


**Fig. 1** Composition of radiography images of bone lesions and defects with classification [case courtesy of Matt Skalski, Radiopaedia.org, rID: 79247]

include cholecystectomy, colectomy, reflux surgery, proctectomy and complex cancer resections [8]. Recent reviews on the robot-assisted surgery include [9–11].

Remodelling and resorption of the bone adjacent the implant is affected by the phenomenon of stress shielding. Where an implant is overly stiff, adjacent bone will be resorbed as it adapts to its new loading conditions. This response known as stress shielding can reduce the bone-implant interface rather than increase it and is particularly apparent for solid metallic biomaterials which tend to have an elastic modulus 10–15 times that of natural bone.

Cellular topologies provide an opportunity to increase surface area for bone cell attachment and to tune the stiffness of an otherwise stiffer-than-bone solid implant material. Biocompatible materials such as stainless steel 316L, cobalt-chromium (CoCr) and titanium (and its alloys) are significantly stiffer and stronger than bone, but when engineered in a cellular form the stiffness and strength are attenuated in relation to their relative density and topology [12]. A cellular solid can be defined as ‘an interconnected network of solid struts or plates which form the edges and faces of cells’, referring to engineered structures or materials, as well as those seen abundantly in nature such as trabecular bone, wood and even honeycombs [13].

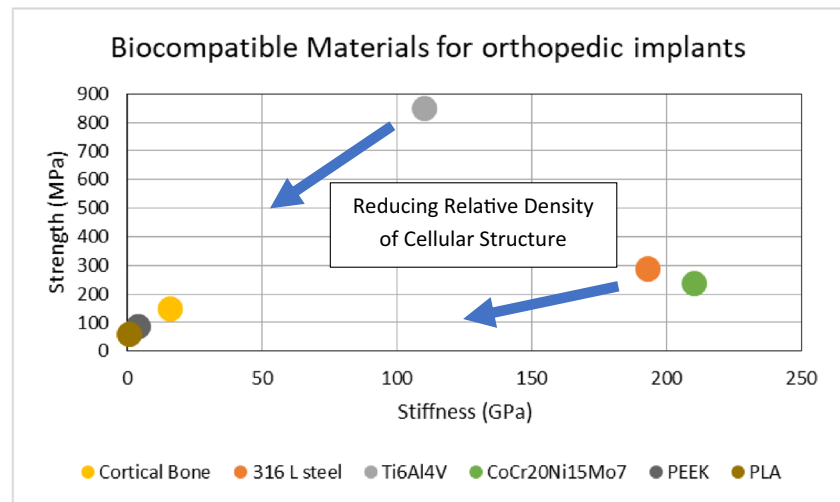
The stiffness and strength of cellular material are typically reduced from that of the parent material; the reduction is dependent on the topology (or connectivity) of the unit cells and the relative density of the structure. If the solid biocompatible material is significantly stronger or stiffer than human bone, then the use of the biocompatible material in a cellular structure could achieve an intermediate strength or stiffness between the solid material and bone. If

the biocompatible material is similar or lower in strength or stiffness than bone, the use of cellular geometry will further reduce strength and stiffness (Fig. 2). Of these materials, Ti6Al4V with high stiffness and strength clearly shows the largest ability to tune stiffness while not overly compromising strength.

Previous studies have been conducted using AM implants in bone defect animal models; however, these studies tend to be in smaller animal models with segmental defects or utilise cylindrical implant designs. Gu et al. [16] reviewed a total of 46 studies on AM porous Ti6Al4V scaffolds for long bone repair in animal models. Forty of the 46 (87%) studies reviewed designed cylindrical implants, and rabbit models were the most common (54%). The larger animal models included sheep, dogs, goats and pigs. A small portion of these studies utilised a ‘femur-shaped’ design (4 of 46), referring to a conformal implant design that matches the geometry of defect; however, all those reviewed were in small animal models (rats). An example of which is the research of Van der Stok et al. [17]; two different titanium lattice implant designs were fabricated to fill a 6-mm segmental defect in the diaphysis of a rat femur. Both implant designs conformed to the removed bone segment with a dodecahedron unit cell topology lattice; however, the designs differed due to their strut diameters (120 and 230  $\mu\text{m}$ ). Twelve weeks post-implantation the femurs were harvested, and their bending test were conducted. The fusion strength reached 62% and 45% of the contralateral femur (intact) for the 120  $\mu\text{m}$  and 230  $\mu\text{m}$  strut diameter lattice implant femur, respectively.

The effect of implant pore size was studied by Taniguchi et al. [18]; LB-PBF was used to manufacture commercially pure titanium lattice implants of cylindrical and plate-like

**Fig. 2** Biocompatible solid materials and the cellular structure. Based on data from [14, 15]



shapes. The tested average pore sizes were 300, 600 and 900  $\mu\text{m}$ , and lattice consisted of a diamond unit cell topology. For mechanical testing of ingrowth strength, the titanium lattice plates were implanted in the metaphysis of the tibia in mature male Japanese white rabbits. Detaching tests were performed on the plate-like implants, involving a tensile load applied to the implant while the anterior cortex of the bone was fixed until plate detachment occurred. The 600  $\mu\text{m}$  pore size implant was recommended due to the balance of bone ingrowth and high fixation ability of the porous structure.

Wieding et al. [19] designed two custom lattice implants for the treatment of 20 mm long segmental defects in the mid-diaphysis of sheep metatarsal bones; the implants themselves were stabilised via commercial osteosynthesis plates. Twelve and 24 weeks postoperatively, the treated metatarsal bones were harvested and mechanical testing as well as the analysis of newly formed bone was performed. Torsional, shear and fracture properties were investigated alongside CT scans for bone mineral density analysis. After 12 weeks, the mechanical properties of the treated bones were approximately 50% of that of the untreated bone. The shear strength, which was derived by modelling the bones cross-section as a hollow ellipse, increased from 30 to 50% during the 12- and 24-week postoperative period.

Overall, the study of patient-specific lattice implants to treat bone defects has been focused on segmental defects or cylindrical implant designs for the study of bone ingrowth and mechanical properties. In this research, a hemi-cortical defect with complex geometry is studied in the femur of sheep. The sheep femur defect model is aimed at mimicking the removal of a bone tumour with tight surgical margins to reduce healthy bone loss. The defect itself has a geometry in which robotic excision was the most feasible approach to simulating the defect. Lattice and solid-based implants are designed to augment the treated bone, and implant fixation

is designed into the implant itself via thru holes for bone screws.

### 1.1 Measurement of implant fixation

The assessment of implant stability may be achieved by invasive and destructive methods or through non-invasive and non-destructive methods [20]. Invasive and destructive methods include:

- Histomorphometric analysis—which evaluate bone-implant interface through dyeing the bone specimen and determine measures such as the bone-implant contact (BIC) ratio and bone-implant interface (BII) which measure the length of contact within a 2D cross-section [21].
- Push-out/pull-out/push-in test—these tests are similar but not equivalent, the pull-in and push-out tests both aim to determine a shear behaviour, while the push-in test also contain a compressive component [22]. The idealised push-out test is done using a cylindrical implant placed transcortically and with force applied parallel to the interface to determine shear strength [23]. Complex bone and implant shapes may require bespoke conformal fixtures to improve alignment and reduce lateral bending [24].
- Tension test—these tests were developed to investigate the tensile strength of the bone-implant interface and measure the force to detach the implant with a tensile stress applied to the interface and create a predominantly adhesive fracture. A disc-shaped implant is placed on cortical bone and bone regrowth is allowed on the flat surface but impeded by PTFE on the edges. It removes some of the compounding factors of other test configurations but the implant is not loaded [25].
- Removal torque analysis—the removal torque can be measured for implanted screws or as a fundamental shear

test using a flat disc implant. In the case of screws, the removal torque is known to be dependent on screw diameter and on surface conditions [26].

A survey of literature studies on implant surface roughness effect on BIC, removal torque and push-out test strength. The survey indicated that there is a positive trend between surface roughness and BIC, with 6 of 16 studies showing statistically significant positive trend, while the remainder did not show a trend significantly different from zero. The biomechanical test was split between removal torque and push-out tests. All five push-out tests showed positive trend for push-out test strength with roughness, three of which were significantly different from zero. The survey found mixed results for removal torques with roughness, with only three of nine studies showing a statistically significant (positive) result [27].

Non-invasive and non-destructive methods to assess implant stability include [28]:

- Radiography analysis and imaging—used to assess quantity and quality of bone, such as bone mineral density (BMD), and changes over time. Techniques include radiography, magnetic resonance imaging (MRI), dual energy X-ray absorptiometry (DXA), computed tomography (CT) and peripheral quantitative computed tomography (QCT) [29]. Course resolution images do not distinguish between bone and marrow, thereby reporting an ‘apparent bone mineral density’. Higher resolution imaging systems allow cortical and trabecular bone to be separately identified. Strong correlation between radiography images and histomorphometric analysis has been reported; however, the CT was not able to distinguish between new bone growth and bone graft or ceramic substitutes [30].
- Insertion torque measurements—can be used to predict primary stability of dental implants and implant screws at the time of implantation, but cannot assess new bone growth. To achieve better stability, osseointegration and reliability, the insertion torque should be decided by a number of factors including the screw geometry and the patient’s bone density [31].
- Modal analysis—measures natural frequency response and attenuation to external steady state or transient impulse forces. Correlation between CT determined bone density and resonance frequency analysis have been shown for dental implants [32]. The vibration response shows increase in energy transmission as the interface bonding increases as demonstrated with curing of an epoxy adhesive [33].
- Surgeon perception—when inserting the implant the surgeon can qualitatively assess the resistance and identify hard stops as indicating implant stability.

The feasibility of using non-destructive micro-computed tomography ( $\mu$ CT) for assessing osseointegration has been compared with traditional histomorphometry [30]. The method involved determining bone-to-implant contact ratio (BIC) as the measure of osseointegration from both the  $\mu$ CT and histomorphometry. To reduce the effect of artefacts in the  $\mu$ CT impacting the BIC measurement, one voxel layer was excluded at the interface. A strong correlation was found for implant only group ( $p=0.09$ ), a moderate correlation for  $\beta$ -TCP/hydrogel preparation group ( $p=0.35$ ) and weak correlation for rhBMP-2 loaded  $\beta$ -TCP/hydrogel preparation group ( $p=0.56$ ). Furthermore, it was reportedly difficult to distinguish low mineral bone from other soft tissues in the  $\mu$ CT, while these were clearly distinguishable in histology.

A study of titanium screw-shaped implants in rabbit tibia revealed continued bone remodelling and increasing removal torque with time (up to 12 weeks) [34]. The mean removal torques increased from 83 Nmm at 3 weeks to 158 Nmm at 6 weeks and 199 Nmm at 12 weeks after insertion. The conversion of the removal torque,  $T$ , to shear strength,  $\tau$ , was through the equation:

$$\tau = \frac{T}{\pi d l r_1} \quad (1)$$

where  $d$  is the mean diameter of the implant,  $l$  is the length and  $r_1$  is the lever arm [34]. Three different lengths were considered (i) based on the total length of the threaded part, (ii) based on the length of potential cortical contact and (iii) the observed bone-implant contact length from histomorphometrical analysis of the matching pair (not-unscrewed) implants. Determined for the 12-week samples, these three lengths gave shear strength mean values of  $0.6 \text{ Nmm}^{-2}$ ,  $1.9 \text{ Nmm}^{-2}$  and  $14.8 \text{ Nmm}^{-2}$ , respectively.

In a separate study, the diameter of screw implants was found to influence the removal torque with an expected strong correlation with the geometric length of contact and moment arm, but with a secondary effect which suggested that newly formed bone did not contribute substantially to the shear force resistance [26].

Walsh et al. compared the osseointegration of bone onto titanium (Ti) dowel-like implants with either Ti plasma coating for increased roughness ( $R_a=22.9 \mu\text{m}$ ) or hydroxyapatite coating for a surface quality comparable with bone ( $R_a=5.6 \mu\text{m}$ ). They determined that titanium dowels with Ti plasma provided a more robust bone-implant interface than with hydroxyapatite coating, as measured by mechanical testing implants at cortical sites after 12 weeks [23]. Additional investigation using histomorphometry at cancellous sites showed benefits for the HA coating in the presence of 1 mm and 2 mm gaps between implant and bone at 4 weeks. Line-to-line and press-fit conditions did not show significant

difference to the Ti plasma coating. The shear stress,  $\tau$ , calculated from the plug-like push-out tests by [23]:

$$\tau = \frac{F}{\pi \left( \frac{c_1 + c_2}{2} \right) d} \quad (2)$$

where  $c_1$  and  $c_2$  are the cortical thickness on each side of the implant, and  $d$  is the implant diameter. The mechanical tests revealed that the force required to push-out the implant was significantly higher for the titanium plasma coating, resulting in higher energy and higher calculated shear stress at the implant-bone interface.

### 1.2 Simulation of bone implants

There are a variety of methods employed in the numerical models of femoral implants as reviewed by [35]; important findings include:

- Identification of bending loads being the most likely to cause fracture and therefore employing bending loads for simulation. Other loads considered include axial compression and torsion.
- The bone has been considered as isotropic in some cases, anisotropic in others. Some considered the Young's modulus as homogenous, and in some cases it was determined by bone density from CT.
- The interface has been modelled with friction coefficients ranging between 0.2 and 2.0 by some researchers, while others assumed the interface was bonded.
- Generally, von Mises stress was used as the failure indicator; however, recently maximum principal strain has been suggested as a better indicator.

- Although a wide range of methods have been used, comparable results were obtained with each method.

This research uses a numerical model to investigate the effect of stiffness on the implant push-out force for a simulated critical-sized defect and includes data from an animal trial using solid and lattice titanium implants.

## 2 Methods

A numerical model of a push-out test for investigating the interface stresses is described below followed by a case study for implants in sheep femurs including the implant design, surgical procedures and push-out test methods.

### 2.1 Push-out test simulation

A numerical model was developed to investigate the push-out test used to measure the strength of implant-bone interface. The bone was modelled as a thin-walled circular cylinder (24 mm outer diameter,  $D$ , and 2.5 mm thickness,  $t$ ) with a resection taken with elliptical cylindrical cut perpendicular to the bone. The cut's cylinder axis is tangent to the outer diameter of the bone and the ellipse major axis aligned to the bone axis. The ellipse major and minor diameter were  $d_1 = 24$  mm and  $d_2 = 8$  mm, respectively. The resected region was filled by an implant geometry which was conformal to the resection cut and the outer diameter of the bone (Fig. 3). The elastic modulus of the implant was adjusted to produce different stress fields at the bone-implant interface. The interface was assumed to be a perfect bond, treated as surface-to-surface contact with rough condition, preventing

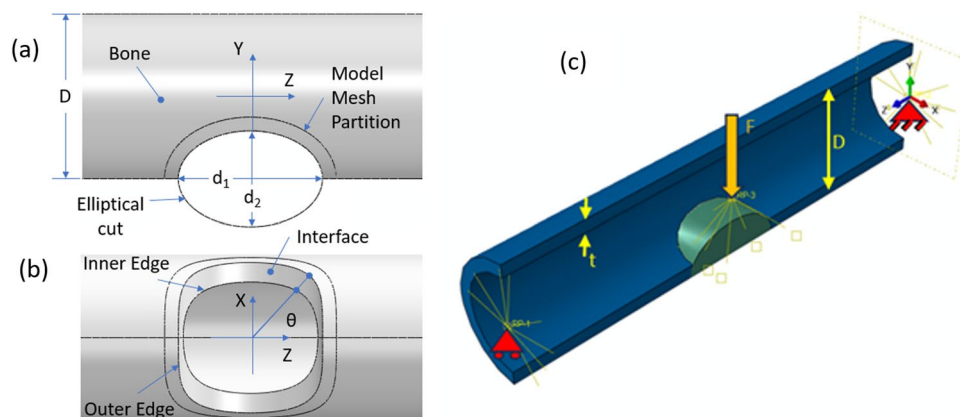


**Fig. 3** Bone and implant geometry with resection and implant based on a straight wall cylinder with elliptical cross-section. Bone side view (a)—showing circular tube bone with elliptical cut geometry. Bone bottom view (b)—showing interface with inner and outer edges, along with angular position  $\theta$ . Cut-away view of the implant-

bone interface model geometry (c), cortical bone represented by thin-walled cylinder (diameter,  $D$ , and thickness,  $t$ ). Reference points and distributing couplings control the simple support boundary conditions at the ends and the push-out load ( $F$ ) applied to the back face of the implant

sliding and allowing contact shear and normal stresses to be identified.

## 2.2 Bone and implant stiffness

The stiffness of the cortical bone and the stiffness range for the implant were based on published Young's modulus data (Table 1). For the investigation, the implant stiffness was considered to range between 0.1 and 10 times that of the bone, representing highly porous polymer and solid metal implants, respectively.

The stiffness of the sheep bones in experiments is based on conversion of CT Hounsfield measurements to bone density for one cross-section and then using the formula  $E = 2065\rho^{3.09}$  [36] with an average value  $1.84 \text{ g/cm}^3$ , providing a cortical bone Young's modulus of 14 GPa.

The numerical models used Abaqus standard implicit solver under a fixed displacement of the implant load reference point. The model used first order hexahedral elements throughout the bone and within 2.5 mm of the interface. The internal region of the implant was generated with tetrahedral elements. An element convergence study for stresses at the interface led to a local element size of 0.5 mm. Contact stress data was extracted for the inner and outer edges. Then, the reaction force at the implant was scaled to produce peak contact pressure indicating fracture of the bone at the interface.

## 2.3 Patient-specific implant design

To test the findings from the simulation model, experimental push-out test results were obtained for an implant study which included solid and lattice implants within sheep [38]. Patient-specific implants were produced via LB-PBF (SLM Solution 125) from Ti6Al4V ELI powder provided by SLM Solutions. Implants were designed to fill a simulated hemi-cortical bone defect in the lateral of the right distal femur. Two implant variants were designed, a solid and a lattice, with each having three distinct regions: the flanges, a primary region and secondary region (Fig. 4).

The overall dimensions of the primary and secondary implant regions are identical across all implants, as the resection geometry (simulated bone defect) is reproduced on each sheep femur in the animal experiment (Sect. 2.4). The primary region of the solid implant variant is designed as a solid titanium section that tapers into the proximal and distal flanges. For the lattice implant variant, the surface of the primary region volume serves as the geometric boundary for a gradient face-centred cubic with Z-strut (FCCZ) lattice structure with a unit cell size of  $4 \times 4 \times 4 \text{ mm}$ . The struts of the unit cells that protrude the primary region are redesigned to conform to the volume's surface; additional conforming vertical, horizontal and diagonal struts are also added to the surface intersecting unit cells. The strut diameters of the primary region lattice structure are linearly graded from 1.4

**Table 1** Bone and implant material properties

Model material	Young's modulus	Reference
Cortical bone (sheep femur)	14 GPa	Calculated
Cortical bone (human femur)	17 GPa	[15]
Titanium implant (solid)	110 GPa	[15]
Titanium implant (lattice rel. density 58%)	11 GPa	Extrapolated [37]
Simulation implant stiffness range	1.4–140 GPa	This study

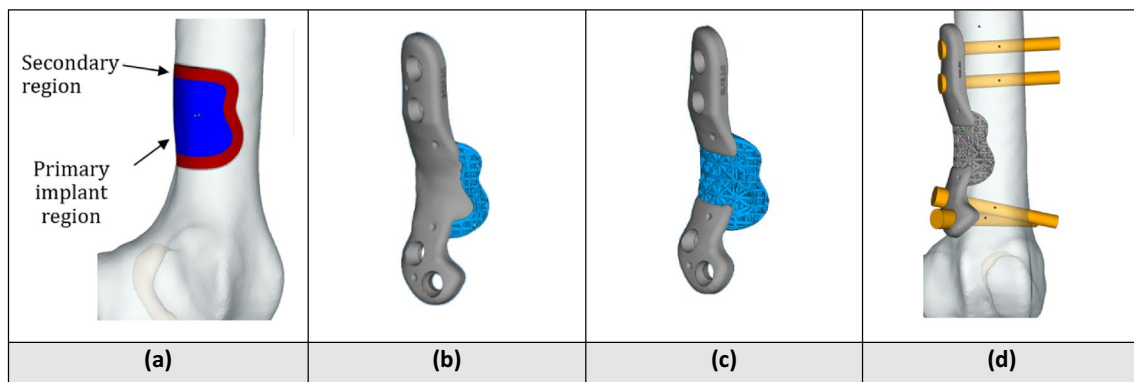


**Fig. 4** Primary and secondary implant regions (a). The solid implants (b) and lattice implants (c) differ by the topology in the primary region, with the same lattice structure employed in the secondary region. Four screws were used to anchor the implant at the flanges (d)

to 0.65 mm based on their distance from the flange regions to reduce thermal distortion.

Both implant variants have identical secondary regions and consist of a FCCZ lattice structure with unit cell size of  $2 \times 2 \times 2$  mm. The secondary region lattice serves as a porous ingrowth layer that interfaces with remaining section of the bone. The strut diameters of the ingrowth layer lattice are also graded, dependent on their distance from the solid flanges, with a maximum and minimum diameter also of 1.4 mm and 0.65 mm, respectively.

The relative density of the lattice implant design is approximately 58%. There are not many examples of lattice mechanical properties reported above 30% relative density; extrapolating from the meta-data reported in [37] suggests the relative modulus for the lattice implant exceeds 10%.

The flanges are used for fixation of the implant, with two separate sections that are located proximally and distally to the bone resection (simulated defect). Both flange sections are designed to be 4 mm thick and linearly taper to a thickness of 2 mm as they intersect the primary implant. The proximal flange has two 4 mm diameter countersunk holes designed to accommodate Stryker AxSOS3 3.5 mm cortical bone screws. The distal flange has two 4.5 mm diameter countersunk holes designed to accommodate Stryker AxSOS3 4 mm cancellous screws. The surface of the flanges that contact the bone are designed to conform to each specific femur and is guided by X-ray computed tomography (CT) to ensure full contact. Edges on the bone contacting side also have a 0.5 mm fillet on sharp corners.

## 2.4 Animal experiment

Previous publications provide the details of the lattice topology selection [39], robot cutting, surgery and animal monitoring [38]. In summary, twenty-four adult male sheep were used in the animal study, treated according to requirements for animal wellbeing and welfare approved by the University of Melbourne animal ethics committee [Ethics ID: 2021–10442–14222–5]. Prior to surgery, the sheep femurs

were scanned via CT and surgery planned. Under anaesthetic, the right femurs were operated to simulate tumour removal, using a supervised automated cutting mode, enabling high precision and repeatability of the resection (implant placement accuracy  $1.05 \pm 0.53$  mm; mean orientation error  $2.38 \pm 0.98^\circ$  [38]). A titanium implant, either solid or lattice, was inserted into the cut bone and secured with four screws. At 12 weeks post-operation, CT was repeated, the sheep euthanised and both left and right femurs were harvested. One group used for histology analysis and another group for mechanical testing.

## 2.5 Biomechanical test overview

To investigate the mechanical properties of the patient-specific AM implants, a combination of non-destructive and destructive tests were performed on a total of 13 right and 17 left femurs that were harvested from 17 approximately 2.5-year-old healthy male sheep cadavers. Nine of the 13 right femurs had implants for 26 weeks prior euthanasia and harvesting. The remaining four right femurs had implants post-euthanasia and are referred to as ‘time-zero femurs’. Of the 17 left femurs, nine were contralateral to the 26-week implant femurs, four were contralateral to the time-zero femurs and the remaining four were contralateral femurs from a previous histology cohort. Table 2 shows the overview of the various bone specimens, implant types, implanted time, number of specimens and the type of tests performed on each. The 26-week implant femurs were subject to non-destructive axial and torsional tests prior to destructive push-out testing. Figure 5 displays descriptive statistics of the bone length, as well as the range and average maximum and minimum calliper diameters measured perpendicular to the femur’s anatomical axis.

All mechanical tests, including the push-out test, were carried out on a universal testing machine (Instron 5969, Instron Corporation, MA, USA) with a 50 kN load cell mounted to the machine’s crosshead (Table 2).

**Table 2** Overview of biomechanical test design. (DT) refers to destructive tests. Histological samples not included

<i>Bone specimen</i>	<i>Implant type</i>	<i>Implant period (weeks)</i>	<i>Number of specimens</i>	<i>Test types</i>	<i>Used in this investigation</i>
Right femur	<b>Solid</b>	<b>26 weeks</b>	<b>6</b>	<b>Axial, torsion, push-out (DT)</b>	<b>Y</b>
Right femur	<b>Lattice</b>	<b>26 weeks</b>	<b>3</b>	<b>Axial, torsion, push-out (DT)</b>	<b>Y</b>
Right femur	Solid	0 weeks	3	Axial, torsion (DT)	N
Right femur	Lattice	0 weeks	1	Axial, torsion (DT)	N
Left femur	Control	0 weeks	4	Axial, torsion (DT)	N
Left femur	Control	Unaltered bone	13	Axial, torsion (DT)	N
Right femur	Control	Unaltered bone	4	Axial, torsion (DT)	N

**Fig. 5** Femur dimensions, normalised bone length and calliper diameter

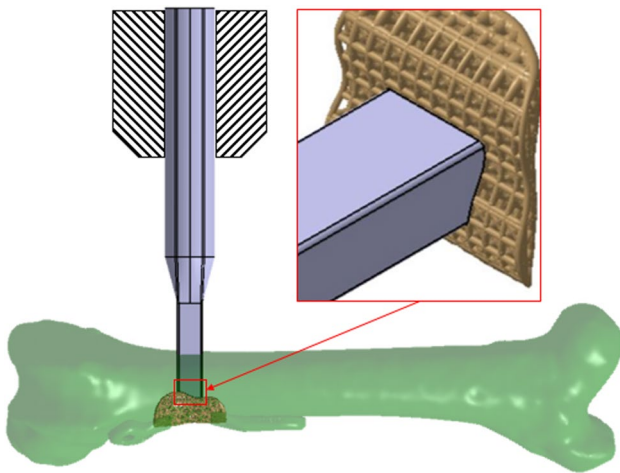
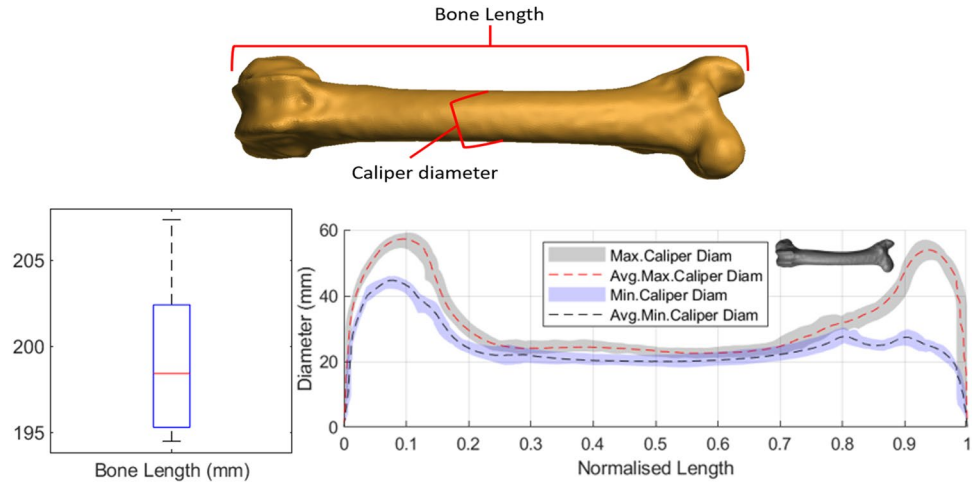


**Fig. 6** Push-out test arrangement and (inset) custom load applicator interfacing with implant

The axial and torsional tests are discussed in a separate publication. The current paper deals only with results of the push-out test.

**2.5.1 Push-out test**

Biomechanical push-out tests were performed on nine of the 6-month harvested femurs (Table 2) to evaluate the effectiveness of bone ingrowth on each implant variant. A custom-test rig was developed to maintain anatomical axis of each femur perpendicular to the custom load applicator. Both sets of cortical and trabecular screws were removed from the implant flanges so that the strength of the bone-implant interface could be tested. A hole was drilled through the medial cortex of the femur in line with the centre of the primary implant region, to enable the load applicator to apply a force directly to the bone interfacing side of the implant (Fig. 6).

The load applicator itself is manufactured via LB-PBF; the contact surface is designed to conform to the surface of the implant at the middle of the secondary implant region. The rectangular section of the applicator is 12 × 8 mm that tapers from a 12 mm diameter cylindrical section; the cylindrical section is firmly held by a set of grips attached to the machine crosshead. The crosshead velocity is maintained at a rate of 1.0 mm/min.

**3 Simulation results**

The surface representing the interface of the implant and cylindrical tube bone were identified in Fig. 3. The interface boundaries are shown as the inner edge and outer edge. Any point on the implant-bone interface edges can be identified by the angle  $\theta$  around the centre point. The angles 0° and 180° align with the bone (tube) axis (Z), while 90° and 270° are transverse aligning to the axis (X).

The implant-bone stiffness ratio,  $\gamma$ , relates the Young’s modulus of the implant,  $E_{\text{implant}}$ , to the Young’s modulus of the bone,  $E_{\text{bone}}$ .

$$\gamma = \frac{E_{\text{implant}}}{E_{\text{bone}}} \tag{3}$$

Figure 7 shows the normal contact pressure and two shear stress components on the bone-implant interface, for  $\gamma=0.1, 1.0$  and 10. For  $\gamma=0.1$ , a relatively compliant implant, the largest tensile forces represented by the minimum contact pressure appear on the inner edge, at the 90° and 270° locations (Fig. 7).

The contact pressure,  $\sigma_n$ , and shear stress components,  $\tau_1$  and  $\tau_2$ , measured at the inner and outer edge of the interface have been extracted and plotted (Fig. 8) as a function of angle,  $\theta$ , around the centre of the implant (Fig. 3). As the implant stiffness is changed between one tenth the bone



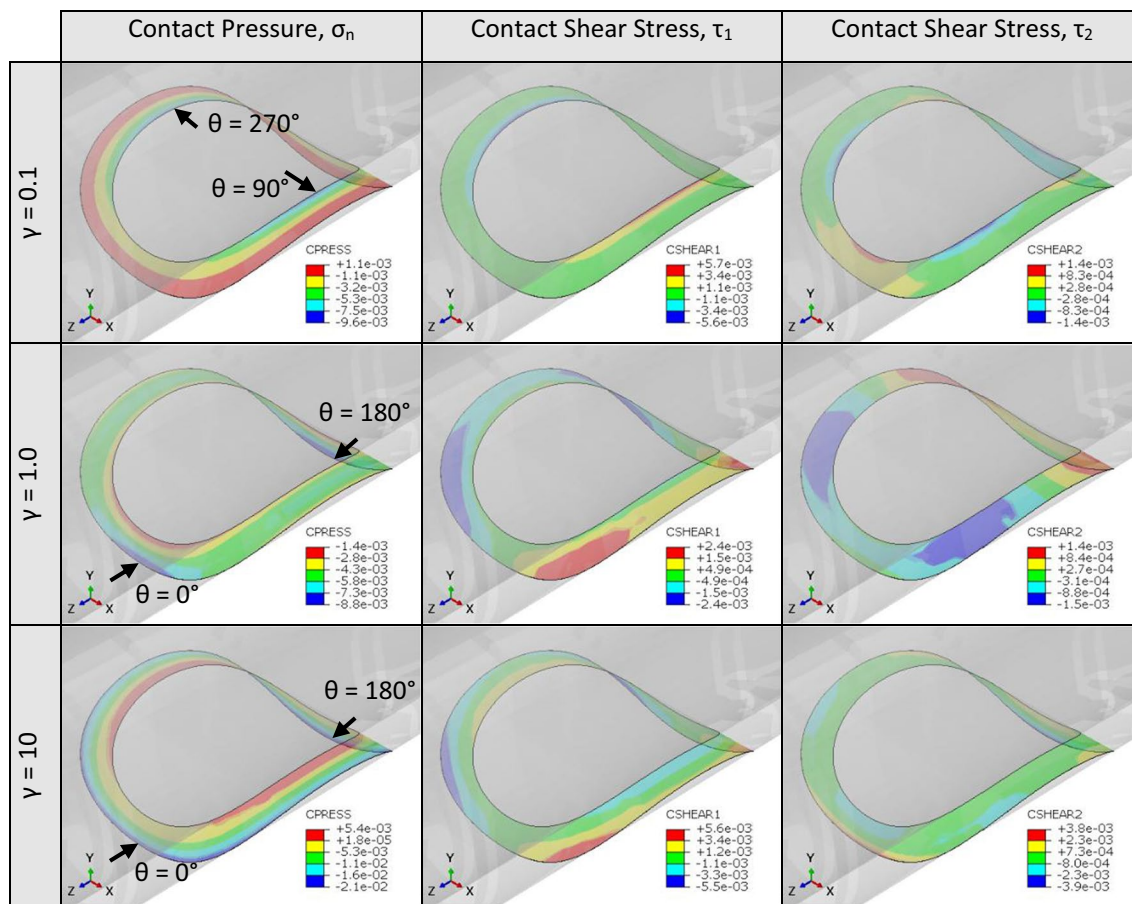


Fig. 7 Interface contact pressure and transverse shear components (MPa) with stiffness ratio,  $\gamma$ . Arrows indicate location of largest tensile stress across the interface (i.e. most negative  $\sigma_n$ )

stiffness to ten times the bone stiffness, the different contact stress components are seen to change. For this work,  $\sigma_n$  has been considered critical as it represents the normal component of the interface reaction, with a negative value indicating a tensile stress which could separate the bone and implant. The curves are plotted when the push-out force causes a  $\sigma_n$  of  $-100$  MPa at either the inner or outer edge, with  $100$  MPa being the ultimate tensile stress for the bone. Some of the important findings from these results are:

- At low implant stiffness ( $\gamma = 0.1$ ), the greatest tensile stress across the interface occurs on the inner edge at the  $90^\circ$  and  $270^\circ$  locations, while the outer edge sees a relatively small stress at the interface. For such a low stiffness implant, the bone-implant interface would expect to fail first at the inner edge at the deepest recess. These results indicate that the low stiffness implant acts as a flexible plug which is pushed out of the bone at relatively low breaking force (Fig. 9) and does not induce large bending stresses. For highly compliant implants, inner edge loading dominates as the outer interface edge is shielded

by the elasticity of the implant. Furthermore, a high variability is observed between the tensile stress recorded at the inner edge, where the interface location closest to the load applicator sees highest stress values (Fig. 8).

- At high implant stiffness ( $\gamma = 10$ ), the greatest tensile stress across the interface occurs on the outer edge at the  $0^\circ$  and  $180^\circ$  locations. Bone strain due to bending is highest away from the neutral axis; concurrently, the highly stiff implant is constrained to attempt to maintain connection at the outer interface. As the stiffness of the implant increases, the tensile stress at the inner interface edge becomes less significant while the outer edge stress continues to dominate. As the implant stiffness increases, breaking force reduces (Fig. 9). Contrary to the low stiffness case, a relatively low variability in interface tensile stress values is observed for the higher stiffness implant. Furthermore, tensile interface stresses on the inner edge interface are relatively low (Fig. 8).
- As the implant stiffness,  $\gamma$ , increases, this plug-like behaviour is reduced and larger bending stresses are created. The tensile stress at the outer edge becomes a more restrictive factor.

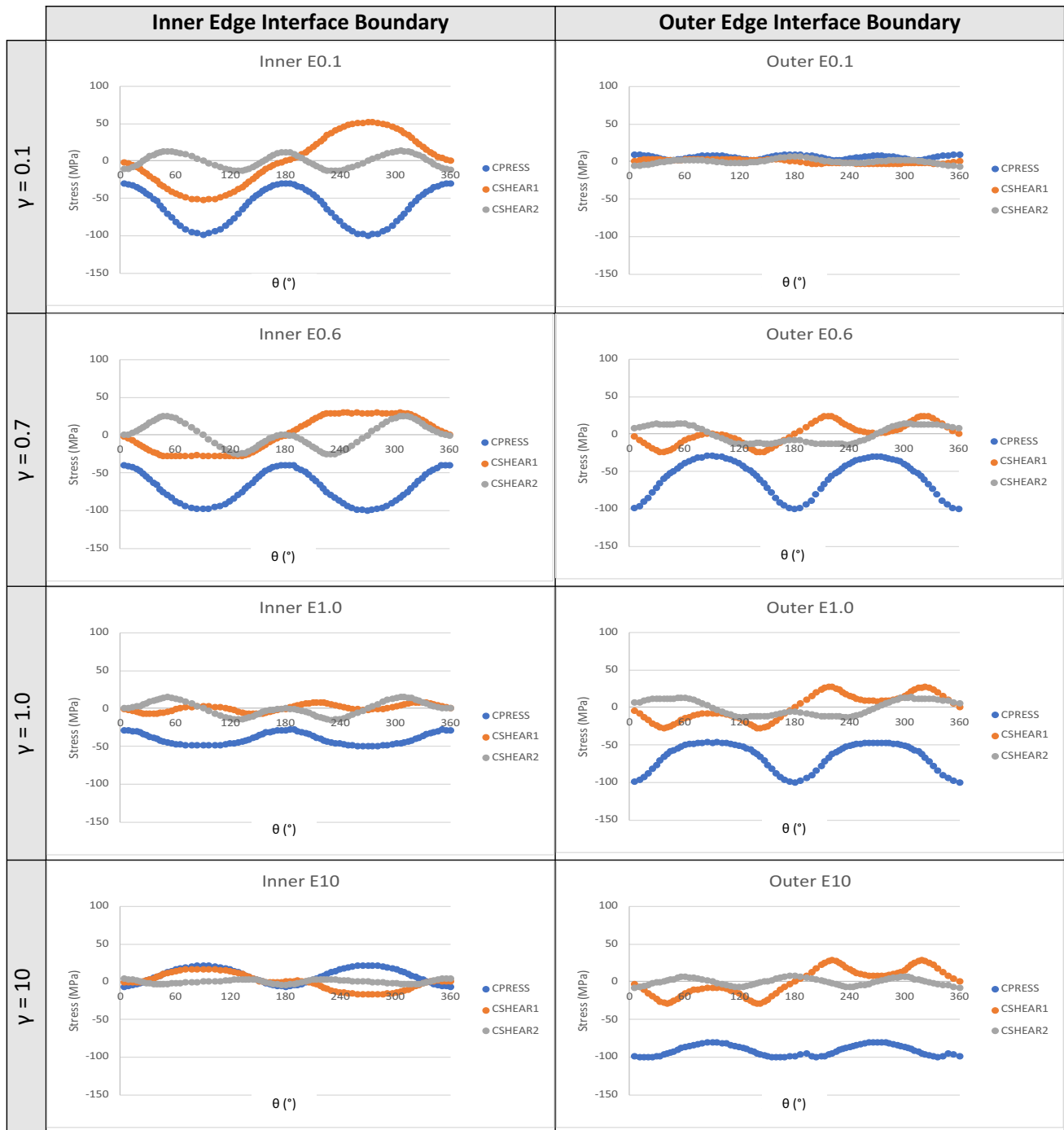


**Fig. 8** Evolution of interface stresses with implant-bone stiffness ratio  $\gamma$  for inner and outer edges. Push-out load scaled such that the minimum  $\sigma_n = -100$  MPa across either boundaries

- For implant stiffness equal to that of the surrounding bone ( $\gamma = 1.0$ ), the observed behaviour is a combination of the low stiffness (plug-like) and high stiffness (bending-induced stress). The maximum tensile stress on the inner interface edge is roughly half the maximum tensile stress on the outer interface edge. Is a more efficient scenario at grounding loads than

for either extremes of low and high implant stiffness. Consequently, at implant stiffness of approximately 0.6–0.7, maximum normal tensile stress at the inner edge ( $90^\circ$  and  $270^\circ$ ) and at the outer edge ( $0^\circ$  and  $180^\circ$ ) become equal. This scenario results in the maximum breaking force observed in this study (Fig. 9).

**Fig. 9** Simulated breaking force with changing implant stiffness. The force to cause a localised 100 MPa tensile stress at the bone-implant interface, assuming complete attachment at bone-implant interface surface. Regions identify the performance of the study lattice (dashed line) and solid implants (solid line)

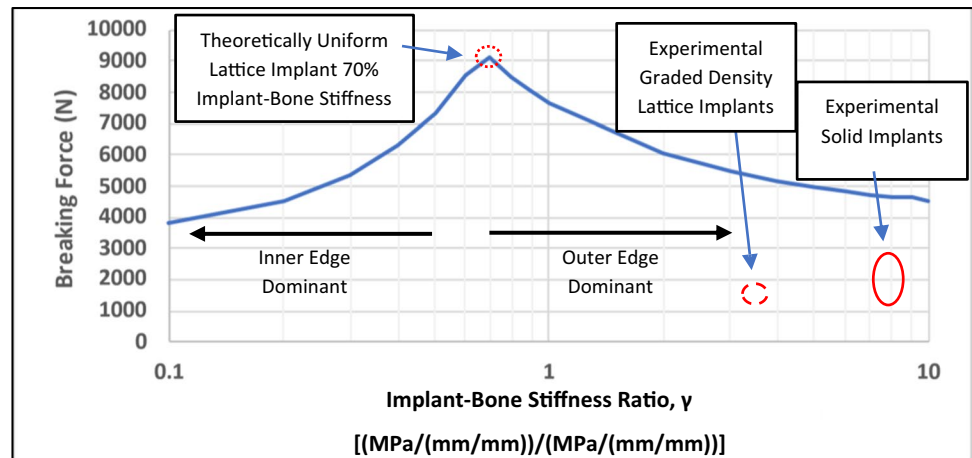
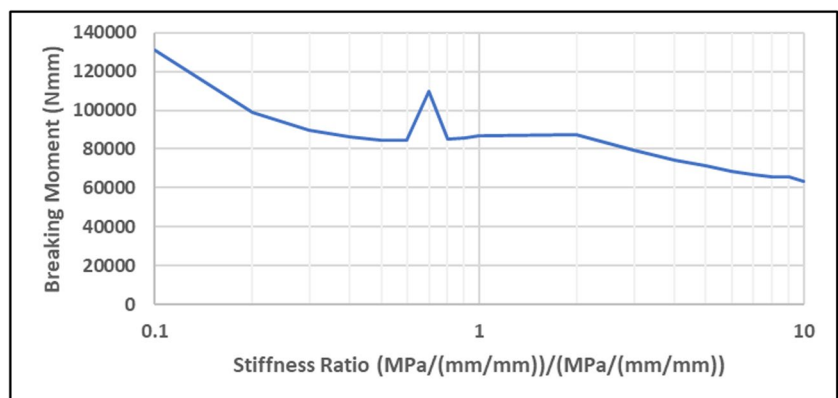


Figure 8 shows how the location of the highest tensile interface stress shifts with the relative stiffness of the implant to bone, without indication of the magnitude of the applied force to cause the interface to fail. Figure 9, however, indicates the applied force to cause a 100 MPa tensile normal contact stress at the bone-implant interface as the implant-to-bone stiffness ratio changes. The curve shows a peak force for the stiffness ratio at which the largest tensile stress (indicated by minimum normal contact pressure,  $\sigma_n$ ) on the inner and outer edge are equal. For the simulated geometry, this occurs at approximately 0.6–0.7 implant-to-bone stiffness ratio.

These results show that the stiffness of the implant affects the local stress (and strain) at the bone-implant interface. A low stiffness implant can lead to high tensile stress at the inner edge of the implant, while high stiffness implants lead to high tensile stress at the outer edge of the implant. For this geometry, an implant with lower stiffness than the bone can increase the breaking force. The exact stiffness at which the plug-like failure and bending-like failure are balanced is likely to be influenced by the geometry of the implant as well as the shape and thickness of the bone.

**Fig. 10** Simulated breaking moment under bending versus stiffness ratio. The bending moment to cause a localised 100 MPa tensile stress at the bone-implant interface, assuming complete attachment at bone-implant interface surface. Note the discontinuity in the region of  $0.6 < \gamma < 0.8$  as discussed in Sect. 3.1

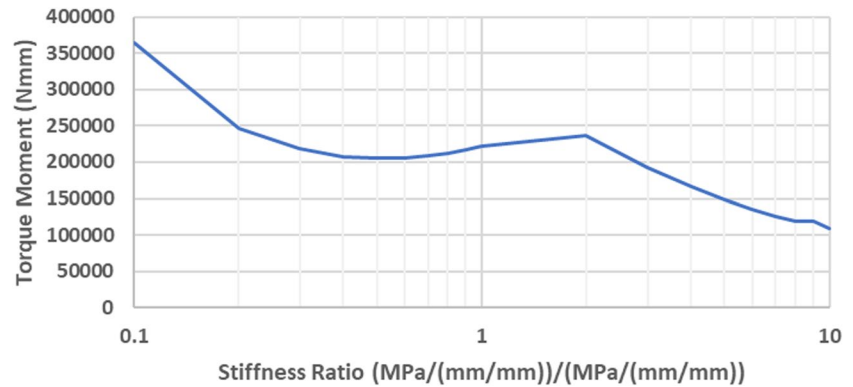


For the sheep study, the solid Ti6Al4V implants have an implant-bone stiffness ratio,  $\gamma$ , of 7.9. Meanwhile, a bulk lattice relative density of 58% gives a relative Young’s modulus of approximately 10% (extrapolated from meta data [37]) giving a  $\gamma = 0.79$ , close to the ideal balance of the two failure modes. However, the increased stiffness of the implant flanges and the large graded strut diameters of the lattice implant (bridging across the implant at  $0^\circ$  and  $180^\circ$ ) means the stiffness ratio of the axially loaded lattice was much higher at  $\gamma = 3.2$ .

### 3.1 Service loading cases

The research focus is the push-out test as a measure of bone-implant integration; however, the same method for analysing the effect of stiffness can be applied to other load cases resembling typical use, such as axial, bending and torsional loads. Figures 10 and 11 show respectively the applied bending moment and torque required to induce the bone ultimate tensile stress at the interface, here referred to as the breaking moment and breaking torque. For the considered implant geometry, both the breaking moment and the breaking torque are high for the very compliant implant ( $\gamma < 0.2$ )

**Fig. 11** Simulated breaking torque versus stiffness ratio. The torque to cause a localised 100 MPa tensile stress at the bone-implant interface, assuming complete attachment at bone-implant interface surface



and low for very stiff implants ( $\gamma > 5$ ). However, they also show a stiffness ratio region ( $0.5 < \gamma < 2$ ) where this trend is reduced or reversed. In this region, the bending response is relatively unchanging, while the torque response shows a local minimum around 0.5 and a local maxima around 2 with approximately a 20% difference in breaking torque. The breaking moment graph also highlights a discontinuity in the region of  $0.6 < \gamma < 0.8$ . Investigation of neighbouring  $\gamma$  values showed breaking moment tending toward two values, indicating some form of instability. This region is near the stiffness ratio for the peak push-out test and could be investigated further to determine the cause.

#### 4 Experimental results and discussion

Experimental implant push-out data is taken from a larger animal study which investigated the histology and load response of solid and lattice implant structures [38]. Nine of the 17 implants were destructively tested for push-out force. It was observed that the implanted structures were not completely separated from the bone following the push-out test. The most common failure mode was that the bones fully break at the site of the implant, with the fracture surface

running along the distal interface surface of the implant and through the load applicator access hole. Furthermore, the distal flange tended to separate from the bone, while with a few exceptions the interface of proximal bone and implant remained intact (Fig. 12). Six of the implant specimens separated in this way, on the distal side of the implant. Sheep 11 and 21 were the only cases to separate on the proximal side of the implant. The fracture of the bone around the implant for sheep 18 was different to other specimens with the fracture incomplete on both sides and a wedge of bone, separated from the rest of the femur, still intact on the side of the implant.

The void regions within the lattice primary region (Fig. 13) show some tissue ingrowth. The bone surfaces at the separated interfaces showed projections matching the lattice voids, indicating bone ingrowth into the secondary lattice region. The skirt of the implant which is common in both the solid and lattice implant was approximately 2 mm in thickness, which is similar to the thickness of the cortical bone, suggesting that the bone ingrowth into the lattice pores which occurred more deeply than the bone surface was likely trabecular rather than cortical bone.

The force–displacement curves for each of the push-out tests (Fig. 14) indicate sheep 15 has the largest

**Fig. 12** Examples of specimens after push-out test. Separation at distal interface (sheep 14) (a), separation at proximal interface (sheep 11) (b), separation at proximal and distal interfaces (sheep 18) (c)

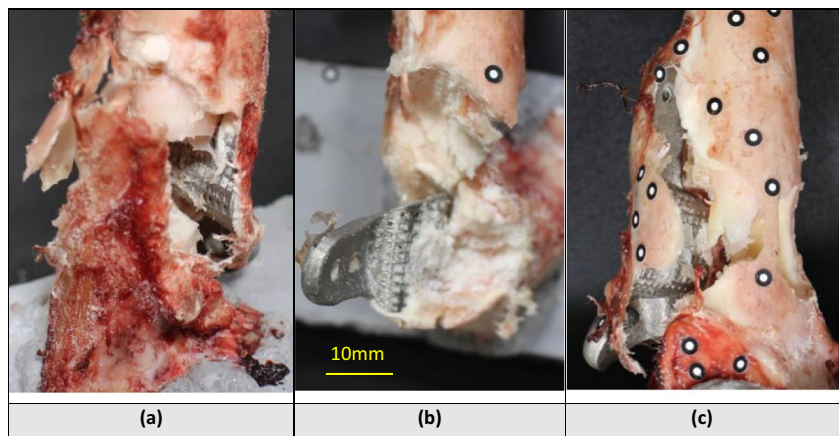


**Fig. 13** Representative images of tissue growth over and into the implants. Including growth of soft tissue over the external flange surfaces (i) and growth of bone within the lattice structure of the primary region (ii). The texture on bone previously interfacing the implant indicating localised bone growth into the lattice voids of the secondary region

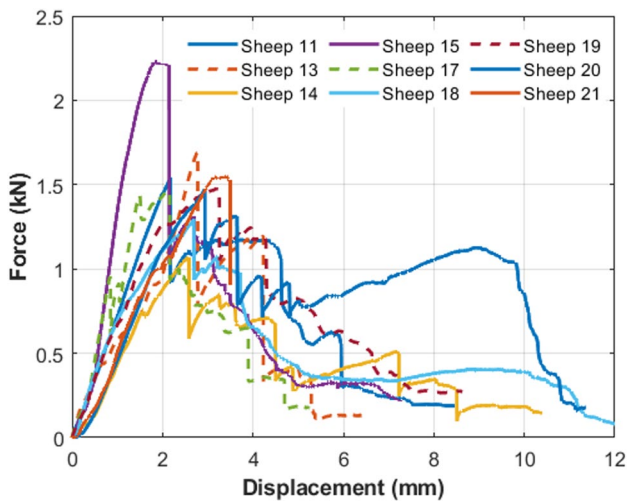
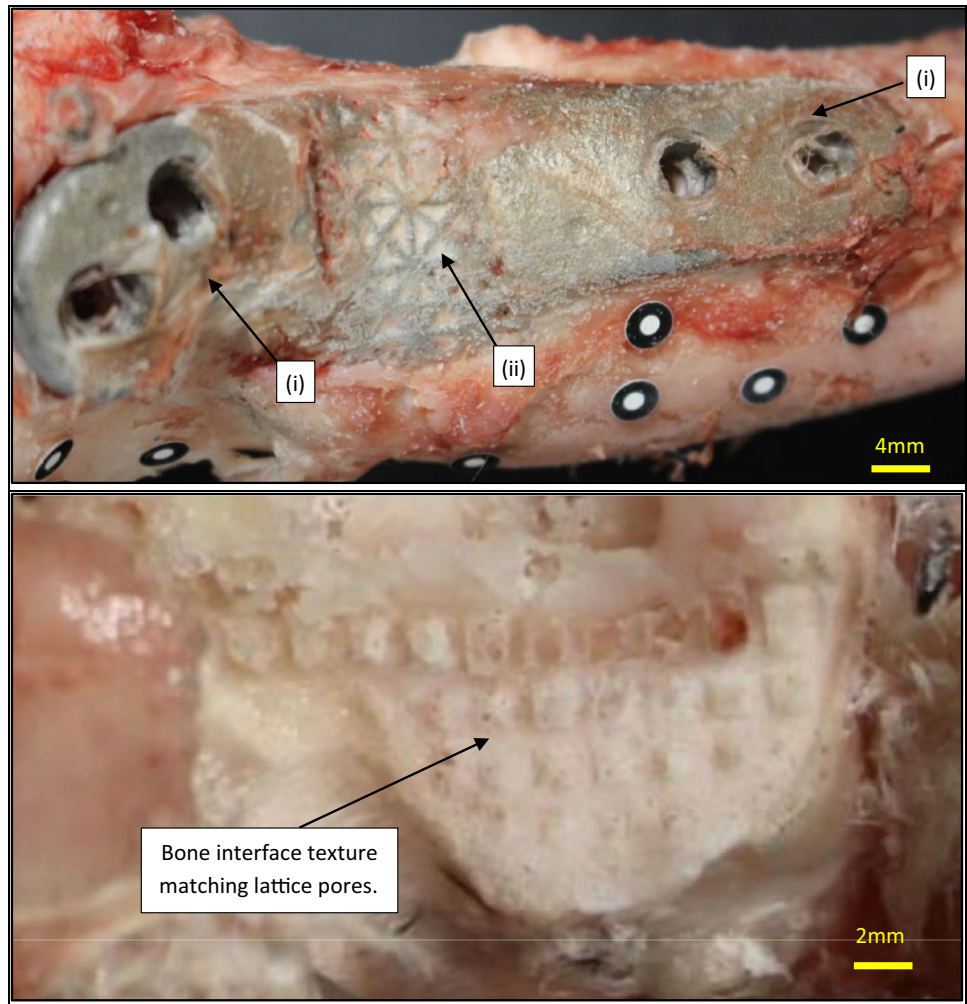


**Fig. 14** Implant push-out test, force–displacement curves. Solid lines for solid implants, dashed lines for lattice implants

push-out force at 2230 N, while the remaining specimens were between 1070 and 1690 N.

Table 3 presents the peak force and displacement at peak force for each of the implant push-out tests. The table also indicates whether the bone break was (full or partial) and which implant–bone interface was exposed after the test (proximal or distal or both). A full break indicates the proximal and distal ends of the bone were no longer rigidly attached to one another, being only connected by soft tissue. Only bones from sheep 17 and 18 had intact bone connection between the upper and lower regions of the bone. The bone diameter was the average measured from  $\mu$ CT cross-sections. It is worth noting the two sheep with the smallest measured femoral diameter also had the two lowest push-out forces. However, sheep 17 which had the largest measured femur diameter had the third lowest push-out force. The table also includes an estimate of the maximum bending stress, calculated assuming a simply supported tubular beam with span 74.5 mm and thickness of 2 mm.

All the interface failure locations were at the  $\theta = 0^\circ/180^\circ$  orientation as predicated by the stiffer than bone implant

**Table 3** Implant push-out peak force and displacement at peak force

Implant type	Solid implants						Lattice implants		
	11	14	15	18	20	21	13	17	19
Specimen ID	11	14	15	18	20	21	13	17	19
Peak force (kN)	1.53	1.07	2.23	1.29	1.47	1.55	1.69	1.46	1.48
Displacement (mm)	2.17	2.59	1.84	2.69	2.94	3.43	2.77	2.11	3.20
Break mode	Full	Full	Full	Partial	Full	Full	Full	Partial	Full
Interface failure	Proximal	Distal	Distal	Both	Distal	Proximal	Distal	Distal	Distal
Bone diam. (mm)	23.5	22.3	23.8	22.2	24.3	22.8	22.7	25.4	24.7
Max bending stress (MPa)	43	34	61	41	38	46	51	34	37

Bone diameter is the mean maximum calliper diameter along the shaft. Maximum bending stress assumes tubular bone cross-section and a simply supported beam

models (Fig. 8). Furthermore, the peak force was 1/4–1/2 the model predicted value which assumes bone fracture at the interface, suggesting that the full bone-implant interface was less than half established.

Statistically, the lattice implant peak push-out forces could not be distinguished from those of the solid implants. In a test for equal variance, the comparisons intervals were seen to overlap, while the multiple comparisons and Levene's test both had large  $p$  values (0.261 and 0.363, respectively) supporting the null hypothesis that all variances are equal. Meanwhile, a main effects analysis revealed only a 0.02 kN (<2%) difference between the group means for the peak push-out force of the lattice and solid implants (1.54 kN and 1.52 kN, respectively).

#### 4.1 Comparison of test with literature

The ideal push-out test is predominantly a shear test enabled by a simple cylindrical geometry for transcortical implants [40]. In this study, the bespoke geometry of the implant was developed to test robotic resection and just-in-time implant development, meaning it required a more complex testing rig. The implemented push-out test induced a significant bending response in addition to the shear response expected of the ideal push-out test. This complicates the ability to compare results from this study with the literature.

For future implementation, the test could be redesigned to reduce some of these effects by removing the flanges to reduce the required span between supports or to change the test from predominantly bending loads to a shear test. Lawson et al. [24] prescribe a push-out test methodology for implants in flat bones (e.g. cranial) which overcome several of the shortcomings of our test.

Alternatively, a pull-out test could also be developed to avoid cutting the bone to expose the back of the implant for a push-out rod. The pull-out test is commonly used for screws, where the implant is significantly stronger than the bone. Unfortunately, the example of a pull-out test applied to a porous structure in [18] was not capable of testing non-load

bearing implants beyond the first 4 weeks after implantation in a small animal model. Therefore, significant redesign would be required for testing of load bearing implants in a large animal model.

#### 4.2 Additive manufacturing and material choice

Additive manufacturing provides the ability to fabricate bespoke cellular structures that are both conformal to the bone resection and functionally graded to meet the stiffness requirements of the bone. The solid and lattice implants used in this study were developed alongside the resection geometry and robot planning to ensure that the implant was conformal with the cut surface of the intact bone. The lattice also featured a reduction in diameter from 1.4 to 0.65 mm varying in proportion to the distance from the flange. Future work could refine the strut diameter distribution within a lattice to match the stiffness of the cortical and trabecular bone.

The lattices were printed in their vertical orientation and did not require support structure beyond anchoring to the platen. It was necessary to ultrasonically clean the lattices to remove loose powder, but no machining or heat treatment was required.

There is a strong case for using Ti6Al4V material for the lattice implants. As seen earlier in Fig. 2, the titanium alloy has significantly higher stiffness and strength than the other biocompatible metals, providing more freedom for tailoring the local lattice topology and density to achieve a stiffness that is comparable with bone, while still having some margin for keeping the strength above that of the bone. Other metals in the graph are stiffer than Ti6Al4V but have less strength to lose. Meanwhile, the polymers shown are below the cortical bone in stiffness and strength, which would be further reduced when fabricated in the form of a cellular structure. However, this stiffness deficit of the polymer materials could be used to advantage with encouraging bone ingrowth, but needs to be done with care to not overly reduce the strength of the implant until the bone can successfully grow into the cells.

## 5 Conclusions

Through numerical modelling of an implant push-out test, it was shown that the push-out force, the failure mode and the crack initiation location are dependent on the stiffness ratio of the implant and bone. A high stiffness implant leads to bending type failure initiating at the outer edge of the implant-bone interface, while low stiffness implants are dominated by the pulling of the implant away from the bone at the inner edge of the interface. The highest push-out force was determined for a stiffness ratio where the inner edge and outer edge tensile stresses are balanced, which for the investigated geometry had a stiffness ratio that was less than 1.0. An experimental study showed that high stiffness solid metal implant and medium stiffness metal lattice implant gave similar push-out force, well below the potential push-out force predicted for a lower stiffness implant.

The push-out test was not the focus of the animal study so did not include the range of stiffness ratio of interest in the numerical study and did not test stiffness ratios that were predicted to require significantly increased push-out force. Further research could investigate the numerical findings using bone replicas, with the interface modelled using adhesive material, before introducing to an animal study.

The implant geometry also influences the overall stiffness of the implant. Further simulation work could explore the effect of parameters relating to the depth and length of the implant. Based on the findings of this study, the implant lattice design was overly stiff for the intended purpose. The implant stiffness could be reduced by reducing the relative density of the metal lattice or by introducing a lower stiffness polymeric material.

**Acknowledgements** The authors acknowledge the facilities and the scientific and technical assistance of the RMIT Advanced Manufacturing Precinct.

**Author contribution** The authors confirm contribution to the paper as follows: study conception and design: D. Downing, D. Shidid, P. Choong, M. Leary, M. Brandt, U. Buehner, S. Ryan, M. Qian; data collection: B. Lozanovski, T. Williamson, A. Namvar, E. Kastrati, D. Hill; analysis and interpretation of results: D. Downing, B. Lozanovski, A. Namvar, M. Leary, M. Brandt; draft manuscript preparation: D. Downing, B. Lozanovski, A. Namvar, M. Leary, M. Brandt.

**Funding** Open Access funding enabled and organized by CAUL and its Member Institutions. The project was co-funded by the Department of Industry, Science, Energy and Resources (Innovative Manufacturing CRC Ltd) and Stryker Australia Pty Ltd (IMCRC/STR/18092017).

## Declarations

**Competing interests** Stryker is a partner in the IMCRC initiative. Dave Hill, Tom Williamson, Peter Choong, Martin Leary, Darpan Shidid and Milan Brandt are co-authors on patents or patent applications related to the technology described in this work. Peter Choong provides consulting work with Stryker. Ulrich Buehner was employed by Stryker

during the period in which this work was completed. Stewart Ryan, Bill Lozanovski, Endri Kastrati, Arman Namvar and David Downing declare that they have no competing financial interests or personal relationships that could have appeared to influence the work reported in this paper.

**Open Access** This article is licensed under a Creative Commons Attribution 4.0 International License, which permits use, sharing, adaptation, distribution and reproduction in any medium or format, as long as you give appropriate credit to the original author(s) and the source, provide a link to the Creative Commons licence, and indicate if changes were made. The images or other third party material in this article are included in the article's Creative Commons licence, unless indicated otherwise in a credit line to the material. If material is not included in the article's Creative Commons licence and your intended use is not permitted by statutory regulation or exceeds the permitted use, you will need to obtain permission directly from the copyright holder. To view a copy of this licence, visit <http://creativecommons.org/licenses/by/4.0/>.

## References

1. Schemitsch EH (2017) Size matters: defining critical in bone defect size! *J Orthop Trauma* 31(Suppl 5):S20–s22
2. Kheirallah M, Almeshaly H (2016) Bone graft substitutes for bone defect regeneration. A collective review. *Int J Dent Oral Sci* 03:247–257
3. Donati D et al (2000) Massive bone allograft reconstruction in high-grade osteosarcoma. *Clin Orthop Relat Res (1976-2007)* 377:186–194
4. Tsuchiya H et al (2005) Reconstruction using an autograft containing tumour treated by liquid nitrogen. *J Bone Joint Surg* 87(2):218–225 (**British volume**)
5. Palmer W, Crawford-Sykes A, Rose R (2008) Donor site morbidity following iliac crest bone graft. *West Indian Med J* 57(5):490–492
6. Bullens P et al (2009) Survival of massive allografts in segmental oncological bone defect reconstructions. *Int Orthop* 33(3):757–760
7. Khan F et al (2013) Haptic robot-assisted surgery improves accuracy of wide resection of bone tumors: a pilot study. *Clin Orthop Related Res* 471(3):851–859
8. Sheetz KH, Claffin J, Dimick JB (2020) Trends in the adoption of robotic surgery for common surgical procedures. *JAMA Netw Open* 3(1):e1918911–e1918911
9. Sayari AJ, Pardo C, Basques BA, Colman MW (2019) Review of robotic-assisted surgery: what the future looks like through a spine oncology lens. *Ann Transl Med* 7(10)
10. Rivero-Moreno Y et al (2023) Robotic surgery: a comprehensive review of the literature and current trends. *Cureus* 15(7):e42370
11. Han J et al (2022) A systematic review of robotic surgery: from supervised paradigms to fully autonomous robotic approaches. *Int J Med Robot Comput Assist Surg* 18(2):e2358
12. Gibson LJ, Ashby MF, Harley BA (2010) Cellular materials in nature and medicine. Cambridge University Press, p 309
13. Gibson LJ, Ashby MF (1999) Cellular solids: structure and properties, 2nd edn. Cambridge University Press, Cambridge
14. Al-Shalawi FD et al (2023) Biomaterials as implants in the orthopedic field for regenerative medicine: metal versus synthetic polymers. *Polymers* 15(12):2601
15. Yang E, Leary M, Lozanovski B, Downing D, Mazur M, Sarker A et al (2019) Effect of geometry on the mechanical properties of Ti-6Al-4V gyroid structures fabricated via SLM: a numerical

- study. *Mater Des* 184:108165. <https://doi.org/10.1016/j.matdes.2019.108165>
16. Gu Y et al (2022) 3D-printed porous Ti6Al4V scaffolds for long bone repair in animal models: a systematic review. *J Orthop Surg Res* 17(1):1–17
  17. Van der Stok J et al (2013) Selective laser melting-produced porous titanium scaffolds regenerate bone in critical size cortical bone defects. *J Orthop Res* 31(5):792–799
  18. Taniguchi N et al (2016) Effect of pore size on bone ingrowth into porous titanium implants fabricated by additive manufacturing: an in vivo experiment. *Mater Sci Eng C Mater Biol Appl* 59:690–701
  19. Wieding J et al (2015) Biomechanical stability of novel mechanically adapted open-porous titanium scaffolds in metatarsal bone defects of sheep. *Biomaterials* 46:35–47
  20. Meenakshi S et al (2013) Implant stability a key determinant in implant integration. *Trends Prosthodont Dent Implantol* 4:28–48
  21. Jackson N et al (2019) Histopathological evaluation of orthopedic medical devices: the state-of-the-art in animal models, imaging, and histomorphometry techniques. *Toxicol Pathol* 47(3):280–296
  22. Seong W-J et al (2013) Comparison of push-in versus pull-out tests on bone-implant interfaces of rabbit tibia dental implant healing model. *Clin Implant Dent Relat Res* 15(3):460–469
  23. Walsh WR et al (2020) Bone ongrowth and mechanical fixation of implants in cortical and cancellous bone. *J Orthop Surg Res* 15(1):177
  24. Lawson ZT et al (2021) Methodology for performing biomechanical push-out tests for evaluating the osseointegration of calvarial defect repair in small animal models. *MethodsX* 8:101541
  25. Xing G, Manon F, Guillaume H (2019) Biomechanical behaviours of the bone–implant interface: a review. *J R Soc Interface* 16:20190259. <https://doi.org/10.1098/rsif.2019.0259>
  26. Ivanoff CJ et al (1997) Influence of implant diameters on the integration of screw implants: an experimental study in rabbits. *Int J Oral Maxillofac Surg* 26(2):141–148
  27. Shalabi MM et al (2006) Implant surface roughness and bone healing: a systematic review. *J Dent Res* 85(6):496–500
  28. Swami V, Vijayaraghavan V, Swami V (2016) Current trends to measure implant stability. *J Indian Prosthodont Soc* 16(2):124–130
  29. Griffith JF, Genant HK (2008) Bone mass and architecture determination: state of the art. *Best Pract Res Clin Endocrinol Metab* 22(5):737–764
  30. Lyu H-Z, Lee JH (2021) Correlation between two-dimensional micro-CT and histomorphometry for assessment of the implant osseointegration in rabbit tibia model. *Biomater Res* 25(1):11
  31. Joshi S et al (2021) An effect of various parameters on insertion torque to improve the success rate of dental implantation: a review. *Mater Today: Proc* 43:928–934
  32. Sumer AP et al (2013) Assessment of the correlation between bond density and implant stability. *J Clin Med* 30(3):237–240
  33. Lu S et al (2022) Experimental investigation of vibration analysis on implant stability for a novel implant design. *Sensors* 22(4):1685
  34. de Rezende MLR, Johansson C (1993) Quantitative bone tissue response to commercially pure titanium implants. *J Mater Sci: Mater Med* 4:233–239
  35. Galteri G, Cristofolini L (2023) In vitro and in silico methods for the biomechanical assessment of osseointegrated transfemoral prostheses: a systematic review. *Front Bioeng Biotechnol* 11:1237919. <https://doi.org/10.3389/fbioe.2023.1237919>
  36. Wirtz DC et al (2000) Critical evaluation of known bone material properties to realize anisotropic FE-simulation of the proximal femur. *J Biomech* 33(10):1325–1330
  37. Maconachie T, Leary M, Lozanovski B, Zhang X, Qian M, Faruque O, Brandt M (2019) SLM lattice structures: Properties, performance, applications and challenges. *Mater Des* 183:108137. <https://doi.org/10.1016/j.matdes.2019.108137>
  38. Williamson T et al (2023) Robot-assisted implantation of additively manufactured patient-specific orthopaedic implants: evaluation in a sheep model. *Int J Comput Assist Radiol Surg* 18(10):1783–1793
  39. Shidid D et al (2016) Just-in-time design and additive manufacture of patient-specific medical implants. *Phys Procedia* 83:4–14
  40. Kovács ÁÉ et al (2023) Comparative analysis of bone ingrowth in 3D-printed titanium lattice structures with different patterns. *Materials* 16(10):3861

**Publisher's Note** Springer Nature remains neutral with regard to jurisdictional claims in published maps and institutional affiliations.